

## 11. CT SCAN ANALYSIS OF SEDIMENTS FROM LEG 146<sup>1</sup>

Juichiro Ashi<sup>2</sup>

### ABSTRACT

An X-ray computed tomography (CT) scanner for medical treatment was used to acquire high-resolution images of density distribution in marine sediments. Whole-round core samples for this study were collected during Leg 146 from the abyssal plain off Vancouver Island and the accretionary prism off Oregon. Knowledge of the relationship between densities and linear attenuation coefficients of made possible quantitative evaluation of even small volumes of the core specimens. On the basis of this relationship, densities derived from CT scans agree well with measured densities of all the samples irrespective of their compositions. Whereas the bulk density of sediment layers thinner than about 1 cm has been little examined previously, CT scans revealed that thin sand layers are less consolidated, suggesting prevention of dewatering by relatively impermeable adjacent mud layers. Sample disturbance can also be easily detected by CT scan images. Rotation planes formed by drilling appear as sharp horizontal discontinuities in CT scan images. These planes exhibit a density lower than that of the surrounding material in unconsolidated sediments and a higher density in moderately consolidated sediments. Multiple profiles of CT scans enable the effect of differential rotation of biscuits to be removed, and are helpful in understanding complex structures such as bioturbation or wet-sediment deformation.

### INTRODUCTION

Physical properties indicate the origin and deformation history of marine sediments, and strongly influence the transport of thermal and acoustic signals. These properties are of particular interest in accretionary prisms, where lateral tectonic stresses arise from plate convergence and associated vertical thickening results in arcward dewatering. Detailed bulk density and porosity measurements have demonstrated the arcward dewatering during accretion (Bray and Karig, 1985), which are verified by increased velocities across accretionary prism transects (e.g., Bangs et al., 1990). In contrast with the knowledge of these mesoscale structures, there are insufficient data to discuss the relationship between the drainage system and sediment densification at the microscale. During Ocean Drilling Program (ODP) legs, shipboard measurement of sediment density is usually determined on cores at intervals of several decimeters. In this study, X-ray computer tomography is employed to evaluate small-scale variations, and the results are calibrated with discrete physical property measurements.

The internal structure of geological samples can be investigated using X-ray radiography, although high resolution requires slabbed samples about 1 cm thick. However, the X-ray CT technique has the advantage of being a nondestructive method, and it provides much higher resolution images than conventional X-ray radiography (Holler and Kogler, 1990). Use of the CT technique has increased over the last five years (e.g., Kenter, 1989; Kimura et al., 1989; Holler and Kogler, 1990; Inazaki and Nakano, 1993). Soh et al. (1993) used an X-ray CT scan system designed for hard-rock samples to look at drill cores from the Nankai accretionary prism. They revealed an increase of density within certain deformation structures in the specimens. During Leg 146, one whole-round core sample was collected from the abyssal plain off Vancouver Island (Site 888), and nine were re-

covered from the accretionary prism off Oregon (Sites 891 and 892; Fig. 1). Sites 891 and 892 are located landward of the frontal thrust fault of the prism (Westbrook, Carson, Musgrave, et al., 1994).

### METHODS

#### Computed Tomography Scanning

A commercial medical X-ray CT scanner (Toshiba TCT-700S) was used to acquire the CT images in this study. The most common type of medical CT scanner has a Rotate/Rotate scan system. In this system, the X-ray source produces a fan-shaped, collimated, irradiating beam. The beam rotates around the sample with a detector at the opposite side. The CT scan image is mathematically reconstructed using the intensities of the transmitted X-ray beam collected at regular increments of rotation around the sample (Iwai, 1979). The peak of radiation used in this study is 120 kV. The relationship between the intensity of the incident beam  $I_0$  and transmitted beam  $I$  is

$$I = I_0 \exp(-\Sigma \mu D),$$

where  $D$  is the sample thickness and  $\mu$  is the linear attenuation coefficient. The intensity of the transmitted X-ray beam is usually expressed as the CT value that is the ratio of the linear attenuation coefficient  $\mu$  of the material to that of pure water. A two-dimensional black-and-white image is derived from irradiating a slice of finite thickness (1, 2, 5, or 10 mm), and shown on a display or recorded on film; a set of digital data of CT values is also stored on disk. Inazaki and Nakano (1993) developed a digital image-processing system on a personal computer for CT scan data, by which the detailed structure of a specimen can be displayed with a desired shade or color corresponding to the CT value.

The unit volume in which the CT value is acquired depends on the slice width of scanning (1, 2, 5, or 10 mm), although the resolution in a profile image is smaller than 1 mm square (approximately 0.6 mm square). A 5-mm slice width was used in this study because CT scan images using 2-mm slices were found to be very noisy, probably due to a deficiency in X-ray penetration for moderately consolidated sed-

<sup>1</sup>Carson, B., Westbrook, G.K., Musgrave, R.J., and Suess, E. (Eds.), 1995. *Proc. ODP, Sci. Results, Vol. 146 (Pt. 1)*: College Station, TX (Ocean Drilling Program).

<sup>2</sup>Geological Institute, University of Tokyo, 7-3-1 Hongo Bunkyo, Tokyo 113, Japan.

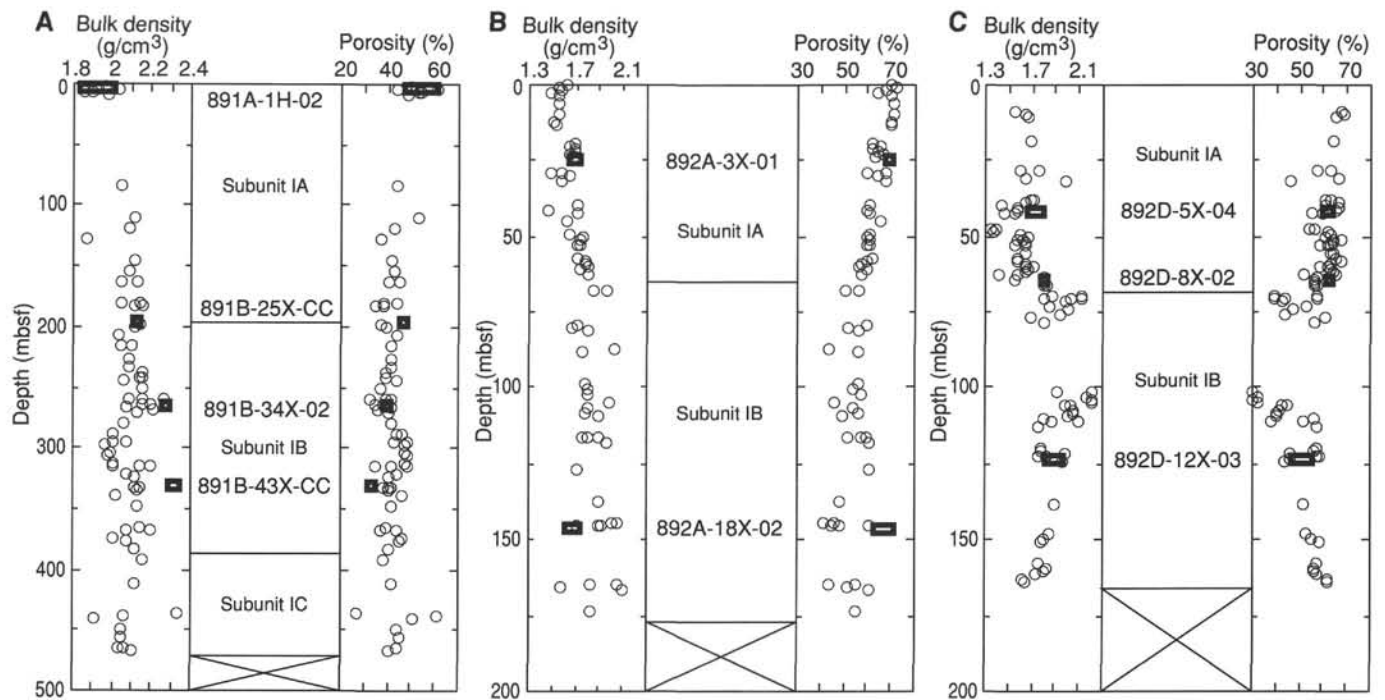


Figure 1. Bulk density and porosity vs. depth for Sites 891 and 892. Circles indicate data derived from shipboard measurements of index properties (Westbrook, Carson, Musgrave, et al., 1994). Rectangles show maximum and minimum values of bulk density and porosity data measured on discrete samples from whole-round cores. A. Holes 891A and 891B. B. Hole 892A. C. Hole 892D.

iments. The unit volume, therefore, corresponds to a cube of about  $0.6 \times 0.6 \times 5.0$  mm. This denotes that measured CT values yield bulk densities averaged over small volumes at the scale of individual grains or grain clusters.

In this study, samples were turned on the core axes and slice images were taken at intervals of  $30^\circ$  or  $45^\circ$ . Black-and-white images from the CT scan were constructed using histogram equalization, which determines brightness windows and ranges, on the image-processing system (Inazaki and Nakano, 1993). Brighter parts in CT scan images, indicating higher CT values, correspond to higher densities. Brightness, however, cannot be correlated among the scans because the windows and ranges used in this study were different in each image. Selected CT scan images of whole-round cores with photographs of core cut faces are shown in Figure 2.

A crossplot of CT values and densities of six standard samples made from clay (bentonite) show a linear relationship (Fig. 3). Conversion of CT values to density was formulated by the best-fit line as:

$$\text{Density} = \text{CT value}/1250 + 1.0 \quad (R^2 = 0.933).$$

Figure 2 shows the density profiles along a core axis line (solid line) and 2 cm to the left (dashed line) and right of it (dotted line), with measured densities for each sample.

### Electrical Resistivity

After CT scanning, electrical resistivity measurements were made on the split core samples. The choice of cutting direction was made according to the CT scan image. The probe and resistivity devices used in this study were designed at the Bedford Institute of Oceanography, and are the same as those used for onboard electrical resistivity measurements during Leg 146 (Westbrook, Carson, Musgrave, et al., 1993). The probe consists of four pins spaced 2.5 mm apart. An alternating current is applied to the outer electrodes, and the resistance of

the sediment between the two inner electrodes is calculated from the measured voltage. Resistivity is defined as the resistance of a unit area across a unit length.

To evaluate anisotropy of resistivity, voltages were applied in both transverse (horizontal) and longitudinal (vertical) directions relative to the core axis, and were spaced at intervals of 0.5 cm or 1 cm. Transverse resistivities were measured sequentially along the center line of the split core and at 2 cm to the left and right; longitudinal resistivities were measured at 1 cm to the left and right of the center line (Fig. 2).

Porosity can be determined using the formation factor (Archie, 1942), which is the ratio of the resistivity of the sediment to that of the pore fluid (assumed seawater), using the following modified Archie's equation (Lovell, 1984):

$$\text{Formation factor} = a \cdot \text{porosity}^{-m},$$

where Archie coefficients  $a$  and  $m$  vary with tortuosity, which is sensitive to grain size and shape, and cementation in sediments, respectively.

### Sediment Index Properties

Samples for index property measurements were collected at intervals of 2 to 6 cm after resistivity measurements. Bulk density was calculated from wet weight and volume using an electronic balance and a Beckman air-comparison pycnometer. After drying for 24 hr at  $105^\circ\text{C}$ , dry weight and volume were measured, permitting calculation of porosity and grain density. Such index property data from split cores provided control data for evaluating CT values and formation factors. This is important because CT values are affected by the absorption rate of the sample materials, and the relation between the formation factor and porosity largely depends on grain size and/or cementation of sediment samples.

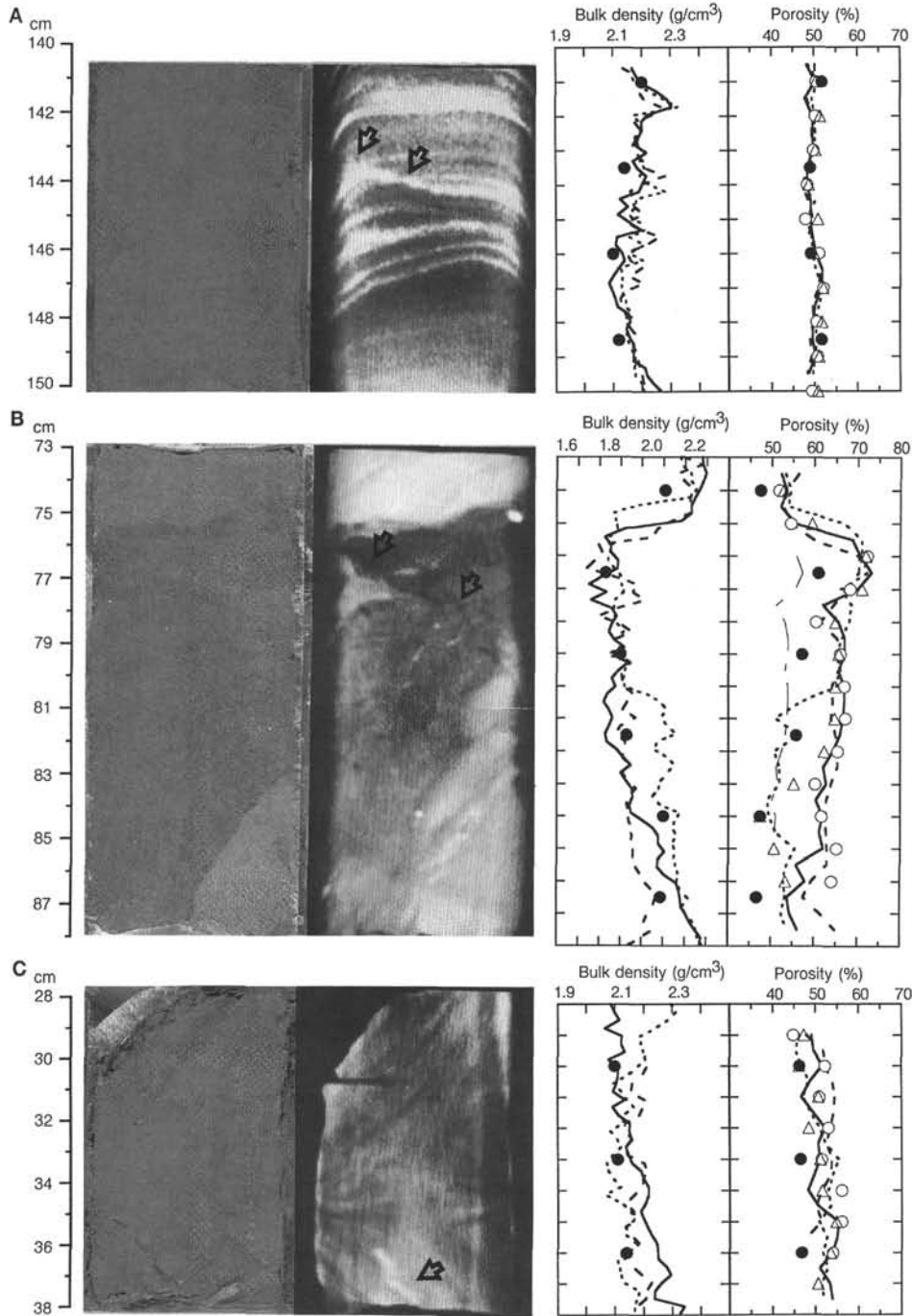


Figure 2. Core photographs, CT scan images, and density and porosity vs. depth. Brighter portion on CT scan image indicates higher density. Three density profiles estimated by CT scans show density distributions of samples along a core axis line (solid line) and 2 cm to the left (dashed line) and right of it (dotted line) with measured bulk density (solid circles). Porosity profiles were estimated from electrical resistivity measurements made in a transverse (horizontal) and longitudinal (vertical) directions. The former measurements were sequentially made along a core axis line (solid line) and 2 cm to the left (dashed line) and right of it (dotted line), and the latter at 1 cm to the left (open circles) and right (triangles) of the core axis. Measured porosities are also shown (solid circles). **A.** Sample 146-888B-14H-3, 140–150 cm. Alternating silt and fine sand layers are cut by a healed fault (arrows) in the CT image. **B.** Sample 146-891A-1H-2, 73–88 cm. Note the healed fault (arrows) in the CT image. The thin dashed line shown in the porosity profile indicates an estimated line based on resistivity using the equation for sand. **C.** Sample 146-891B-25X-CC, 3–13 cm. A composite fold (arrow) is observed in the CT image. **D.** Sample 146-891B-34X-2, 9–13 cm. Note the sigmoidal structures (arrow) in the CT image. **E.** Sample 146-891B-43X-CC, 28–36 cm. The CT image exhibits the healed fault displacing the brighter zone, which corresponds to the silt layer. **F.** Sample 146-892A-3X-1, 137–150 cm. **G.** Sample 146-892D-5X-4, 82–97 cm. Note distributions of sand grains (arrows) showing intense disturbance. **H.** Sample 146-892D-8X-2, 96–112 cm. Bright spots in the CT image correspond to consolidated siltstone fragments. **I.** Sample 146-892D-12X-3, 115–130 cm. Note the subhorizontal high-density zone (arrow) in the CT image. **J.** Sample 146-892A-18X-2, 22–42 cm. Note the healed fault (upper arrow) and the tight fold (lower arrow).

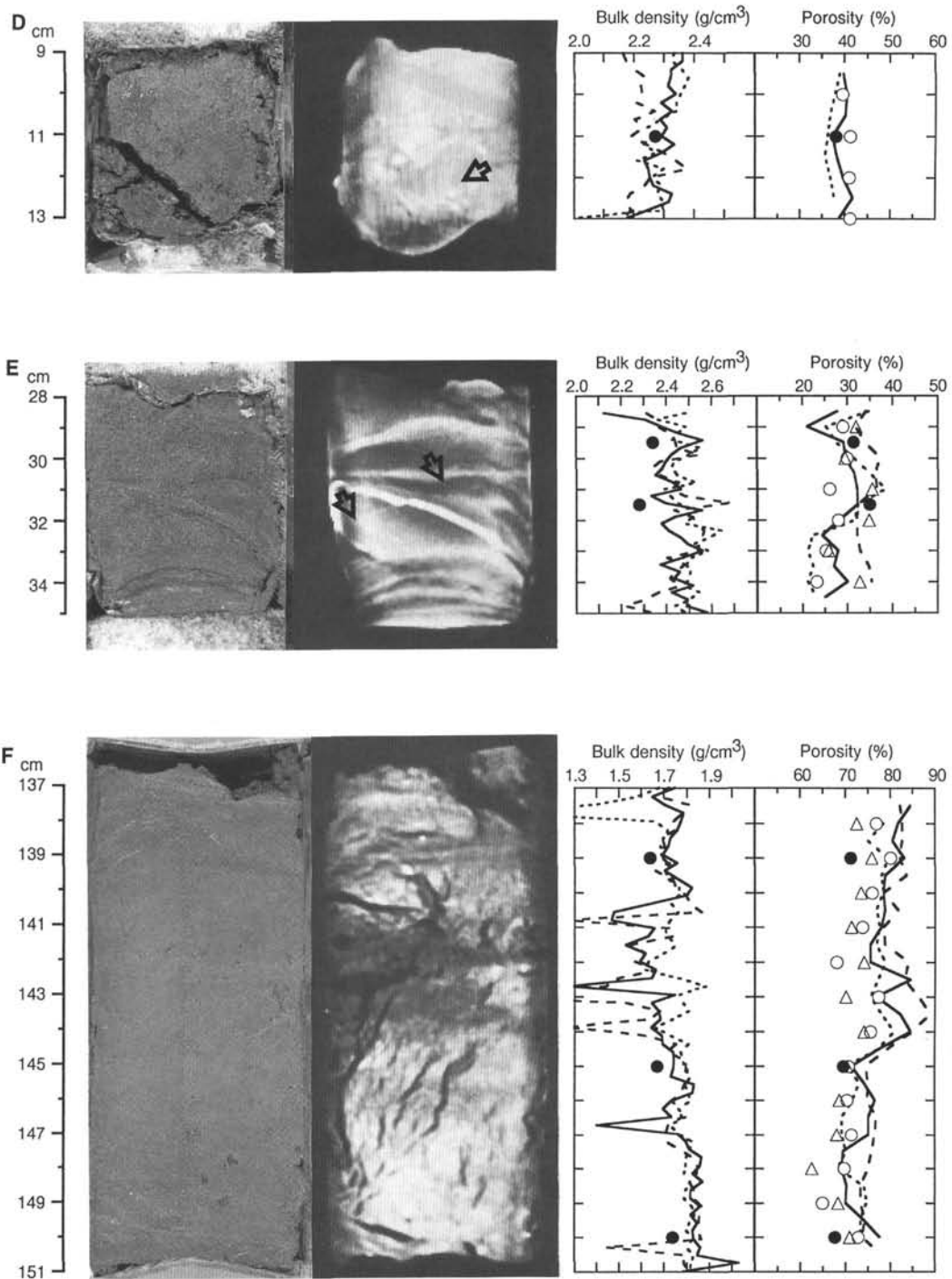


Figure 2 (continued).

## RESULTS

Formation factors calculated from resistivity are crossplotted with measured porosity after core splitting (Fig. 4). Archie's equation, using the coefficients  $a = 1.29$  and  $m = 1.49$  (Lovell, 1984), representative of deep-sea sediments, fits well with the measured porosity data. The maximum 5% discrepancy between the theoretical and measured porosities shown in Figure 4 must be attributed to differences in grain size and/or cementation. The effects of these factors will be discussed for each sample in a later section. In comparison with conventional porosity measurements, electrical resistivity provides fine-scale porosity variations and anisotropy of pore continuity (Fig. 2).

Sample 146-888B-14H-3, 140–150 cm, collected from a depth of 122.5 meters below seafloor (mbsf), consists of silt and a small amount of very fine sand (Fig. 2A). Whereas the core photograph reveals only one thin layer of very fine sand, the CT scan image indicates alternating bright and dark zones, which are interpreted to correspond to clay and silty sand layers, respectively. Moreover, a normal fault clearly displacing the lamination is observed (Fig. 2A).

Sample 146-891A-1H-2, 73–88 cm, collected from 2.23 mbsf, consists of very fine sand interbedded with silty clay. The CT scan image reveals inclined silt layers and a healed reverse fault, whereas the core photograph lacks evidence of both the lamination and the fault plane (Fig. 2B). The contacts between sand and mud exhibit ir-

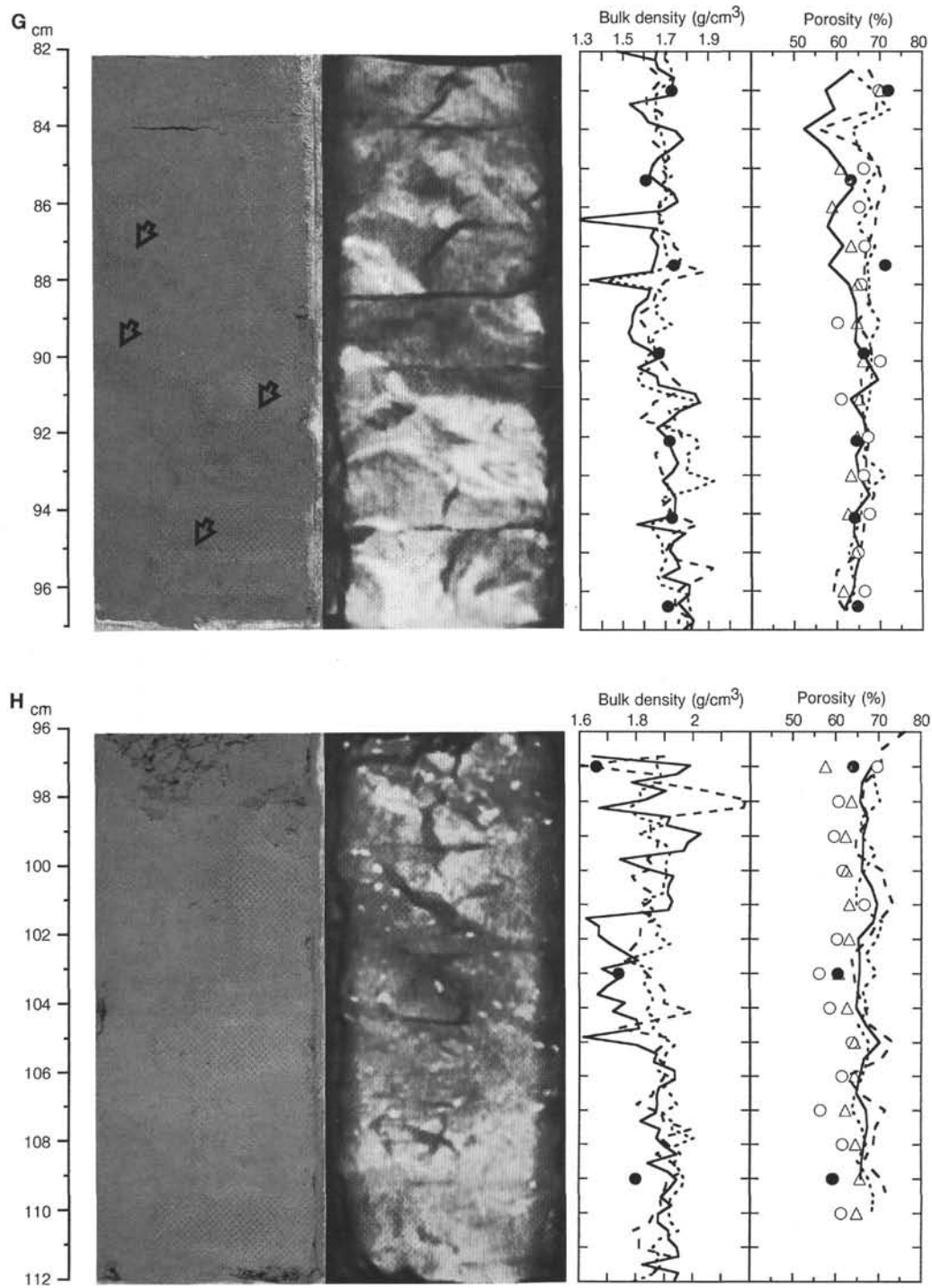


Figure 2 (continued).

regular shapes. These structures may be a suite of wet sediment deformation structures, which were described in Cores 2H and 3H just below this sample during shipboard studies as convoluted, folded, and inclined layers (Westbrook, Carson, Musgrave, et al., 1994). Bulk density is consistent with density estimated from CT scan, but measured porosities in sandy parts show lower values than those calculated from resistivity (Fig. 2B).

Sample 146-891B-25X-CC, 3–13 cm, is located just above the fracture zone between 198 and 278 mbsf (Westbrook, Carson, Musgrave, et al., 1994). CT scan images oriented in various directions re-

veal a foldlike structure, and with this knowledge the core was able to be split in a direction which optimized viewing of the fold. The fold hinge with a subhorizontal axial trace is apparent in the core photograph, and the CT scan image reveals a composite fold at the fold limb (Fig. 2C).

Sample 146-891B-34X-2, 9–13 cm, is located just below the fault (264 mbsf) inferred from geochemical anomalies in pore fluids and gases and is within the discrete fracture zone described on board (Westbrook, Carson, Musgrave, et al., 1994). A core photograph shows a mixture of sand, mud, and soft claystone pebbles. Sigmoidal

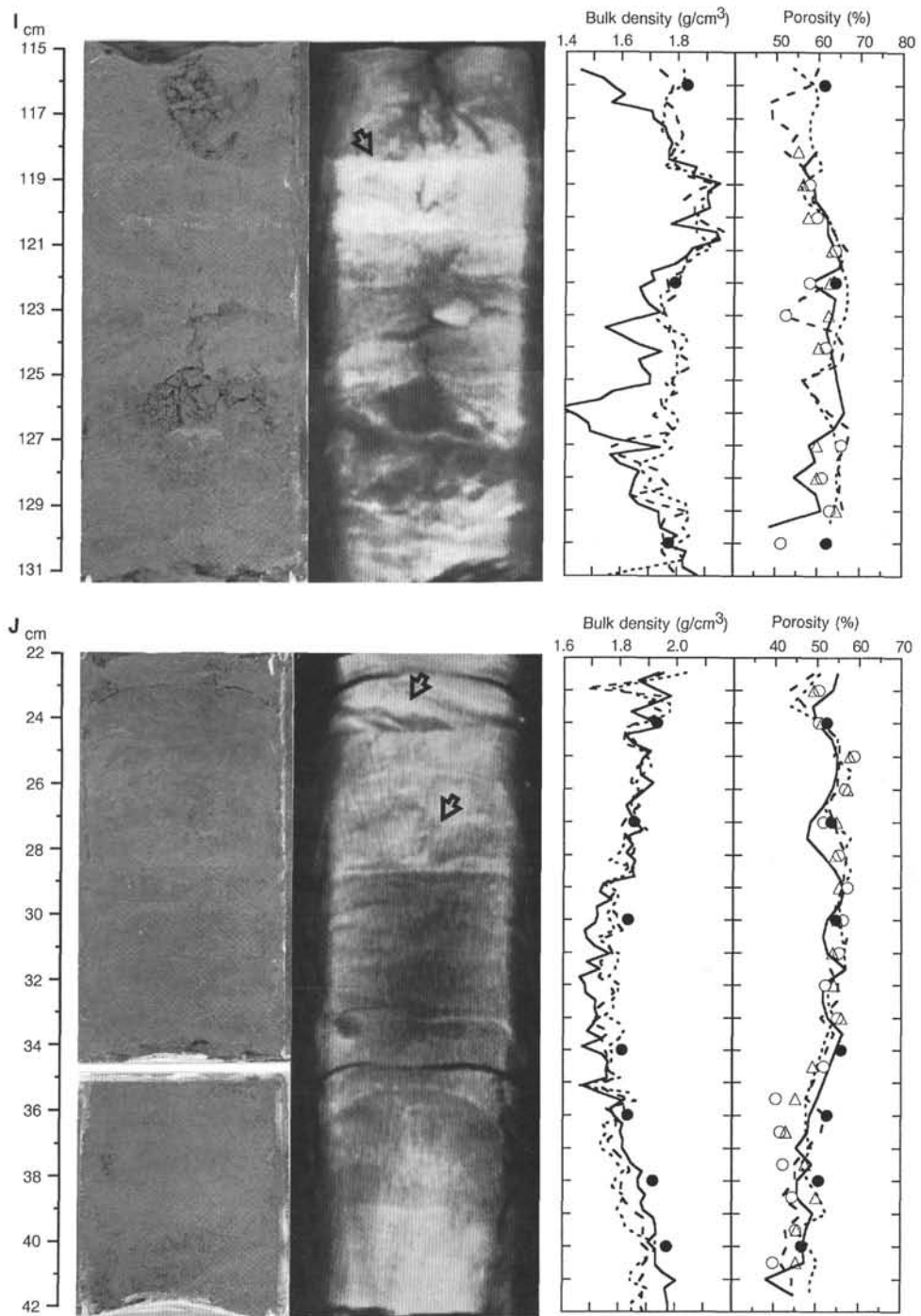


Figure 2 (continued).

structures are observed in the CT scan image (Fig. 2D), but they are insufficiently clear for their origin to be inferred.

Sample 146-891B-43X-CC, 28–36 cm (334.9 mbsf), is composed of fine sand intercalated with thin silt layers (Fig. 2E). The CT scan image shows the silt layers as bright zones corresponding to positive spikes in the density profile, and shows a small fault displacing one of these silt layers (Fig. 2E). The density and porosity values measured in this sample are inconsistent with the general trends of on-

board index property data (Fig. 1). This may be the result of artificial consolidation of the sample, which was obtained from a core catcher.

Sample 146-892A-3X-1, 137–150 cm (19.0 mbsf), is composed of silty clay with a high water content. The CT scan image shows the development of fractures filled by very low density materials, which correspond to negative spikes in the density profile; these fractures do not appear on the split core face (Fig. 2F). Anisotropy of resistivity was detected in the upper half of the sample. This may result from the

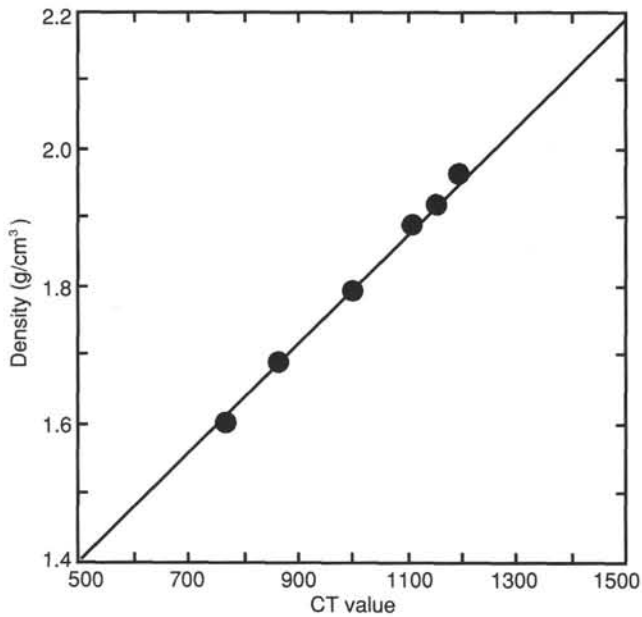


Figure 3. Relationship between bulk density and CT value, which is a ratio of the linear attenuation coefficient of the material to that of pure water, on six standard samples. Conversion of CT values to density was based on this relationship (best-fit line).

distribution of subhorizontal fractures with low resistance. In the lower half of the sample, fractures are well formed at an oblique angle to the two directions of resistivity measurements.

Sample 146-892D-5X-4, 82–97 cm (41.5 mbsf), consists of unconsolidated silt and sand. The core photograph shows ring-shaped distributions of sand grains which correspond to brighter portions in the CT scan image (Fig. 2G). These structures are not interpreted to result from drilling disturbance because drilling-induced horizontal fractures partly cut and rotate them. Spiral shapes revealed by six CT scan images at intervals of  $30^\circ$  suggests that bioturbation is the most reasonable explanation for the origin of these structures. Index properties are consistent with the estimated density and porosity irrespective of sand/silt ratios (Fig. 2G).

Sample 146-892D-8X-2, 96–112 cm, was collected from just below the reverse fault (64.0 mbsf) detected by biostratigraphic age reversal (Fourtanier, this volume) and consists of partly consolidated silty clay. The CT scan image is characterized by dark seams which suggest fractures filled by low-density material and rotations of biscuits along horizontal zones, although the fractures are not evident in the split core (Fig. 2H). The density profile from the CT scan indicates high constant values intercalated by negative spikes (Fig. 2H) that correspond to the fractures. Measured bulk density is lower than the density estimated from the CT scan because of drilling disturbance, as discussed in a later section. Resistivity data in the horizontal direction also show positive spikes, suggesting distributions of porous fractures (Fig. 2H). Resistivity-derived porosities in the vertical direction are in good agreement with the measured porosities, and comparison with the horizontal direction indicates a large anisotropy due to the preferred orientation of fractures.

Sample 146-892D-12X-3, 115–130 cm (122.0 mbsf), consists of consolidated siltstone clasts dispersed in unconsolidated mud (Fig. 2I). The CT scan image is characterized by blocks of various density and by a subhorizontal high-density zone. Highly fractured, consolidated blocks contained in the upper and lower parts of the sample exhibit an unexpected low density. The high-density zone corresponds to the highly disturbed portion and consists of the same materials as

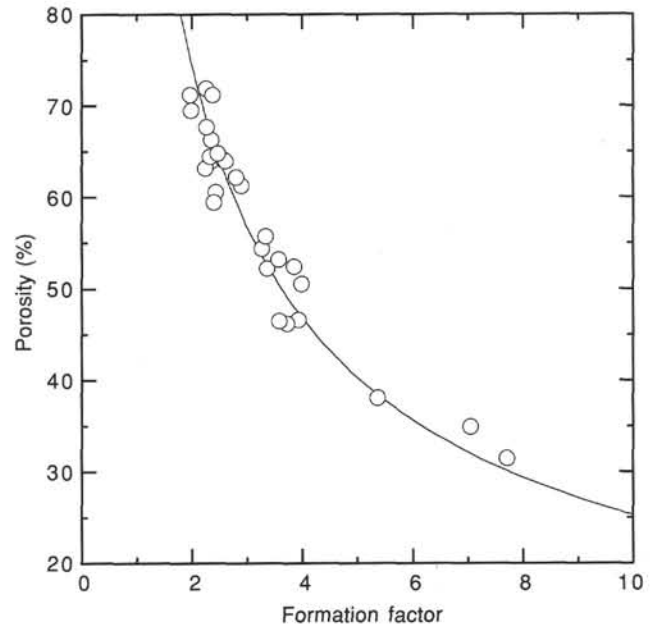


Figure 4. Formation factor vs. measured porosity of this study sample. Coefficients  $a=1.29$  and  $m=1.42$  of Archie's equation (shown by solid line) is in good agreement with this relationship.

the structureless core-rim sediments caused by drilling (Fig. 2I). Measured bulk density and porosity are consistent with estimated values except for the fractured blocks.

Sample 146-892A-18X-2, 22–42 cm, is collected from the lower part of a shear zone (116–147 mbsf) showing melange fabric (Westbrook, Carson, Musgrave, et al., 1994). A core photograph also shows scaly fabrics developed in clayey siltstone (Fig. 2J). Repetition of the same layer caused by a minor reverse fault and a tight fold were observed in the CT scan image (Fig. 2J). These structures are cut by subhorizontal, thin, high-density zones, one of which makes a sharp density boundary. Another type of subhorizontal zone is an open fracture filled by low-density materials. Measured bulk density and porosity are generally consistent with the estimated values (Fig. 2J).

## DISCUSSION

The first question to be discussed is whether the relationship between CT value and density estimated from standard samples can be applied to sediments that include grains of various attenuation coefficients. Comparison of measured bulk densities, derived from sampling portions for index properties, with mean CT values indicates no systematic deviation from the relationship obtained using standard samples (Fig. 5), except for the samples disturbed by splitting, as discussed later. Sample 146-891A-1H-2, 73–88 cm, consists of very fine sand and silty clay having large density variations (Fig. 2B). Density estimated by CT scan, however, indicates a relatively good correlation with measured bulk density without regard to grain size (Fig. 2B). On the other hand, resistivity is very sensitive to grain-size changes; the resistivity-derived porosities are much higher than the discrete measured values in the sand layer (Fig. 2B). In order to convert from formation factor to porosity, the Lovell relation (Lovell, 1984) has been generally applied in this study. However, this equation is suitable strictly for mudstone only. In the case of sand, the coefficients  $a$  and  $m$  in Archie's equation have been estimated to be 0.62 and 2.15 (Asquith and Gibson, 1982). Applying this equation,

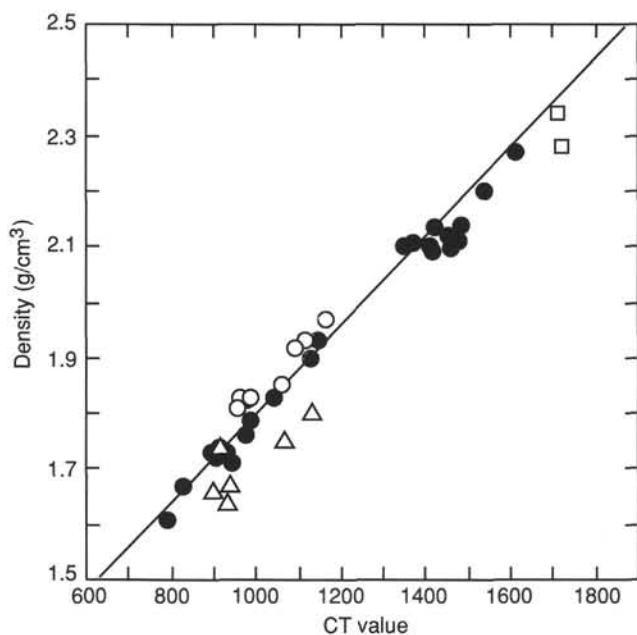


Figure 5. Scatter plot of CT values vs. measured densities, with the best-fit line derived from standard sample measurements (see Fig. 3). Note relatively large deviation from the best-fit line in Sample 146-891B-43X-CC, 28–36 cm (open squares), Samples 892A-3X-1, 137–150 cm, and 892D-8X-2, 96–112 cm (open triangles), and Sample 892A-18X-2, 22–42 cm (open circles). See text for explanation.

the resistivity-derived porosity fits much better with the measured porosity (Fig. 2B).

In view of this negligible effect of composition on estimating density from CT values, CT scanning can yield quantitative data in fine-scale density variations hard to measure by conventional methods. Sample 146-888B-14H-3, 140–150 cm, is composed of very fine sand intercalated with thin silt layers (Fig. 2A). The CT scan image indicates several silt layers, shown as bright zones; the density profile shows that the differences between the silt and fine sand exceed  $0.1 \text{ g/cm}^3$  (Fig. 2A). The relationship between porosity and density is:

$$\text{Porosity (\%)} = (\rho_s - \rho) / (\rho_s - \rho_{pw}),$$

where  $\rho_s$ ,  $\rho$ , and  $\rho_{pw}$  are grain density, bulk density, and pore water density, respectively. Using the measured grain density data ( $2.65\text{--}2.78 \text{ g/cm}^3$ ) and a constant pore water density ( $1.024 \text{ g/cm}^3$ ), density differences between silt and sand correspond to more than a 5% porosity deviation. In Sample 146-891B-43X-CC, 28–36 cm, which mainly consists of fine sand, a higher density is also estimated in silt layers than in sand layers (Fig. 2E), although the sediment may have suffered coring disturbance because the sample was obtained from a core catcher. In a normal sedimentary environment, the porosity of sandy sediment is expected to be lower than that of clayey sediments at the same burial depth. The lower density in this sand suggests that the coarser grained layers might have been prevented from dewatering by adjacent impermeable, fine-grained layers.

The second matter is how to distinguish sediments disturbed by drilling in CT scans. In Sample 146-892A-3X-1, 137–150 cm, the CT-scan-derived density is characterized by nearly uniform values between  $1.6$  and  $1.8 \text{ g/cm}^3$ , with interesting negative spikes to less than  $1.5 \text{ g/cm}^3$  (Fig. 2F). The latter are interpreted to reflect fractures filled by sediments with very high water content, such as muds remo-

bilized by drilling. Measured bulk densities smaller than those estimated for the interbedded sediments from the CT scan suggest that discrete samples contained some low-density, fractured material. These structures appear to be continuous with the porous material at the core rims, and are attributed to drilling disturbance. A similar relationship is observed in Sample 146-892D-8X-2, 96–112 cm, where the CT-scan-derived density shows relatively constant values of about  $1.9 \text{ g/cm}^3$  and negative spikes less than  $1.7 \text{ g/cm}^3$  (Fig. 2H). Measured bulk density reflects an average of the two materials. The anisotropy of resistivity in this sample (Fig. 2H) might have been caused by pervasive small-scale horizontal fractures due to drilling disturbance.

Sediments modified by drilling are also likely to be disturbed during core splitting. Samples 146-892A-3X-1, 137–150 cm, and 892D-8X-2, 96–112 cm, which include low-density, fractured material as mentioned above, show low bulk density in comparison with CT values (Fig. 5), suggesting development of low-density portions by splitting. Sample 146-891B-43X-CC, 28–36 cm, which mainly consists of fine sand, has a lower bulk density without fractures. This may result from fluidization during core splitting (Fig. 5). In the case of Sample 146-892A-18X-2, 22–42 cm, all measured bulk densities are higher than CT-scan-derived densities (Figs. 2J and 5). The increase of measured bulk density is probably caused by the loss of pore water at pervasive microfractures, observed after core splitting in the scaly clay (Fig. 2J). The resistivity-derived porosity is consistent with measured porosity because both sets of data were acquired after core splitting.

In most cases, sediments disturbed by drilling exhibit low densities in the CT scans, but thin horizontal zones characterized by density higher than the surrounding material are observed in Sample 146-892A-18X-2, 22–42 cm (Fig. 2J). In Sample 146-892D-12X-3, 115–130 cm, aggregation of thin horizontal zones makes a 2-cm-wide high-density zone (Fig. 2I). This kind of densification is interpreted to result from mechanical consolidation during drilling. In consolidated blocks within the same sample, the density profile estimated from the CT scan shows abnormally low densities of about  $1.4 \text{ g/cm}^3$  (Fig. 2I), because microfractures not filled with pore water reduce CT-scan-derived density. Fragmentation within partially consolidated blocks is interpreted to be produced by drilling even as mechanical consolidation occurred along the biscuit boundary. By these patterns, drilling disturbance can be easily distinguished on CT scans.

Multiple profiles of CT scans permit removal of the effect of differential rotation of biscuits. The minor reverse fault observed at the top of Sample 146-892A-18X-2, 22–42 cm, is cut by a horizontal biscuit boundary (Fig. 2J). CT scan images at various angles suggest the rotation angle along this plane is about  $180^\circ$ . After reorientation by this amount, the sense of shear on the drag fold observed in the lower biscuit coincides with the displacement sense of the minor fault. Paleomagnetic measurements were also attempted on this sample, but unstable and weak remanent magnetization prevented the reconstruction of original directions. Electrical resistivity measurements indicate no anisotropy, in spite of the shear fabrics.

## SUMMARY AND CONCLUSIONS

Using an X-ray CT scanner designed for medical treatment, high-resolution images of density distributions in cored samples were obtained on unsplit cores. The resolution of CT scanning is down to about a 0.6-mm-square image section and allows a 5-mm depth for beam width. This nondestructive technique is effective for determining the optimum cutting direction, for observing internal structures, and for examining whole-round cores used in other experimental studies.

This study found that the effect of differences in composition on the relationship between CT value and bulk density was negligible in

all samples. This may be due to low variations in composition in samples of this study. Density and porosity estimated by CT scan and resistivity, respectively, are generally in good agreement with the shipboard measurements of physical properties. In addition, this CT scan study provides high-resolution density data that cannot be acquired by conventional methods. For example, thin (<1 mm) sands interbedded with mud have lower density than pure mud layers. This suggests that coarser grained layers embedded with clayey layers might have been prevented from dewatering by impermeable fine-grained layers.

Electrical resistivity measurements are also useful for estimating porosity distributions at ranges smaller than the centimeter scale, although the measurements involve the risk of sample disturbances during core splitting. Anisotropy of resistivity can provide significant information about fabrics of marine sediments, but further work is necessary to evaluate the effects of disturbances by drilling and splitting.

Sample disturbance is well detected in CT scan images. In unconsolidated sediments, biscuit boundaries and other drilling-induced deformation show abnormally low densities. In moderately consolidated sediments, on the other hand, thin zones of biscuit boundaries with a higher density than the surrounding sediments tends to develop. In both cases, drilling disturbances are easily distinguished from original structures. One problem for estimating density from CT scanning arises in fine-scale, fractured sediments because the CT scan data averages densities of the void portions with the rest of the sediment.

Multiple profiles of CT scans can represent the three-dimensional shapes of structures, and enable the effect of differential rotation of biscuits to be removed. For example, bioturbated sediments (such as Sample 146-892D-5X-4, 82–97 cm) and the relationship between the minor fault and the fold in the probable tectonic shear zone (Sample 146-892A-18X-2, 22–42 cm) were well-recognized by this CT scan study. In these ways, CT scanning offers several advantages over examining sediments by conventional techniques, and provides a valuable additional tool.

### ACKNOWLEDGMENTS

I acknowledge the assistance of the SEDCO crew and the ODP technical staff. I wish to thank K. Moran for information regarding the electrical resistivity device. Critical reviews and comments by

A.J. Maltman and J.K. Morgan are gratefully acknowledged. T. Inazaki, T. Nakano, and H. Noro provided helpful comments about digital image processing. I am also indebted to Y. Inouchi and M. Shida for technical support in the use of the CT scanner. Thanks are due to Toshiba Medical, Inc., for permission to use the CT scan data format.

### REFERENCES

- Archie, G.E., 1942. The electrical resistivity log as an aid in determining some reservoir characteristics. *J. Pet. Tech.*, 5:1–8.
- Asquith, G.B., and Gibson, C.R., 1982. Resistivity logs. In *Basic Well Log Analysis for Geologists*: Tulsa, OK (AAPG), 41–65.
- Bangs, N.L.B., Westbrook, G.K., Ladd, J.W., and Buhl, P., 1990. Seismic velocities from the Barbados Ridge Complex: indicators of high pore fluid pressures in an accretionary complex. *J. Geophys. Res.*, 95:8767–8782.
- Bray, C.J., and Karig, D.E., 1985. Porosity of sediments in accretionary prisms, and some implications for dewatering processes. *J. Geophys. Res.*, 90:768–778.
- Holler, P., and Kogler, F.-C., 1990. Computed tomography: a nondestructive, high-resolution technique for investigation of sedimentary structures. *Mar. Geol.*, 91:263–266.
- Inazaki, T., and Nakano, T., 1993. An image processing system of X-ray CT data for the internal structural analysis of geological specimens. *Geoinformatics*, 4:9–23.
- Iwai, Y., 1979. *CT Scanner—X-ray Computed Tomography Scanner*: Tokyo (Corona-sha Publ.). (in Japanese)
- Kenter, J.A.M., 1989. Application of computerized tomography in sedimentology. *Mar. Geotechnol.*, 8:201–211.
- Kimura, G., Koga, K., and Fujioka, F., 1989. Deformed soft sediments at the junction between the Mariana and Yap Trenches. *J. Struct. Geol.*, 11:463–472.
- Lovell, M.A., 1985. Thermal conductivity and permeability assessment by electrical resistivity measurements in marine sediments. *Mar. Geotechnol.*, 6:205–240.
- Soh, W., Byrne, T., Taira, A., and Kono, A., 1993. Computed tomography (CT) scan image analysis of Site 808 cores: structural and physical property implications. In Hill, I.A., Taira, A., Firth, J.V., et al., *Proc. ODP, Sci. Results*, 131: College Station, TX (Ocean Drilling Program), 135–140.
- Westbrook, G.K., Carson, B., Musgrave, R.J., et al., 1994. *Proc. ODP, Init. Repts.*, 146 (Pt. 1): College Station, TX (Ocean Drilling Program).

**Date of initial receipt: 5 September 1994**

**Date of acceptance: 31 March 1995**

**Ms 146SR-214**